



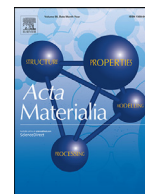
Quantitative predictions of thermodynamic hysteresis: Temperature-dependent character of the phase transition in Pd–H

Downloaded from: <https://research.chalmers.se>, 2025-12-10 01:14 UTC

Citation for the original published paper (version of record):

Rahm, M., Löfgren, J., Erhart, P. (2022). Quantitative predictions of thermodynamic hysteresis: Temperature-dependent character of the phase transition in Pd–H. *Acta Materialia*, 227. <http://dx.doi.org/10.1016/j.actamat.2022.117697>

N.B. When citing this work, cite the original published paper.



Quantitative predictions of thermodynamic hysteresis: Temperature-dependent character of the phase transition in Pd–H

J. Magnus Rahm*, Joakim Löfgren, Paul Erhart

Chalmers University of Technology, Department of Physics, Gothenburg S-412 96, Sweden

ARTICLE INFO

Article history:

Received 14 October 2021

Revised 26 January 2022

Accepted 27 January 2022

Available online 1 February 2022

Keywords:

Thermodynamics

Phase coexistence

Strain energy

Cluster expansion

Hysteresis

ABSTRACT

The thermodynamics of phase transitions between phases that are size-mismatched but coherent differs from conventional stress-free thermodynamics. Most notably, in open systems such phase transitions are always associated with hysteresis. In spite of experimental evidence for the relevance of these effects in technologically important materials such as Pd hydride, a recipe for first-principles-based atomic-scale modeling of coherent, open systems has been lacking. Here, we develop a methodology for quantifying phase boundaries, hysteresis, and coherent interface free energies using density-functional theory, alloy cluster expansions, and Monte Carlo simulations in a constrained ensemble. We apply this approach to Pd–H and show that the phase transition changes character above approximately 400 K, occurring with an at all times spatially homogeneous hydrogen concentration, i.e., without coexistence between the two phases. Our results are consistent with experimental observations but reveal aspects of hydride formation in Pd nanoparticles that have not yet been accessible in experiment.

© 2022 The Author(s). Published by Elsevier Ltd on behalf of Acta Materialia Inc.

This is an open access article under the CC BY license (<http://creativecommons.org/licenses/by/4.0/>)

1. Introduction

Phase transitions involving size-mismatched phases are ubiquitous in materials science. Often such phase transitions are studied with the underlying assumption that the interface between the two phases is incoherent, such that the system is free from stress far from the interface. There are, however, important cases for which this assumption breaks down. Notable examples include intercalation in LiFePO₄ nanoparticles used in Li-ion battery cathodes [1] and hydride formation in Pd nanoparticles. The latter has attracted increasing attention during the last decade, not only because Pd–H is a prototypical system for intercalation of small solute atoms in a host metal, but also due to its technological relevance in hydrogen storage [2], optical hydrogen sensing [3,4], and membrane reactors [5]. Mounting evidence [6–8] suggests that the phase transition from the hydrogen-poor α phase to the hydrogen-rich β phase in Pd nanoparticles smaller than about 300 nm in diameter occurs with a coherent interface between the two phases, in spite of their significant mismatch in lattice parameter. As a consequence, the system exhibits considerable strain, which fundamentally alters the thermodynamics of phase transitions, as first shown in seminal works by Cahn, Larché, and others [9–16]. In par-

ticular, Schwarz and Khachatryan [17,18] have shown that in open systems, the strain energy associated with the coherent interface constitutes a macroscopic energy barrier that is inevitably associated with hysteresis, i.e., a hysteresis mandated by thermodynamics and insurmountable by thermal fluctuations (Fig. 1).

The effort to better understand the dynamics of the phase transition in Pd–H nanoparticles has largely been driven by experiment [19–24], notably including advanced imaging techniques that have revealed the details of the phase transition in time and space [7,8,25]. Due to the challenges associated with transmission electron microscopy at high temperatures, atomic-scale imaging of nanoparticles during the phase transition has, however, generally been limited to temperatures well below room temperature, and thereby much lower than the temperature ranges where hydrogen sensors are required to operate. As we will see below, this is unfortunate given the temperature-dependent character of the phase transition. Meanwhile, modeling of coherent systems has primarily been based on phase-field models and other models with effective free energy expressions [26–32], ground-state data assuming ideal mixing [33] or atomic-scale studies at specific temperatures [34]. At the same time, robust methodologies for first-principles calculations of thermodynamic properties on the atomic scale have remained insufficiently developed. Thus, there have been few or no attempts to quantify important aspects such as the magnitude of the hysteresis and coherent interface energies from first prin-

* Corresponding author.

E-mail addresses: magnus.rahm@chalmers.se (J.M. Rahm), erhart@chalmers.se (P. Erhart).

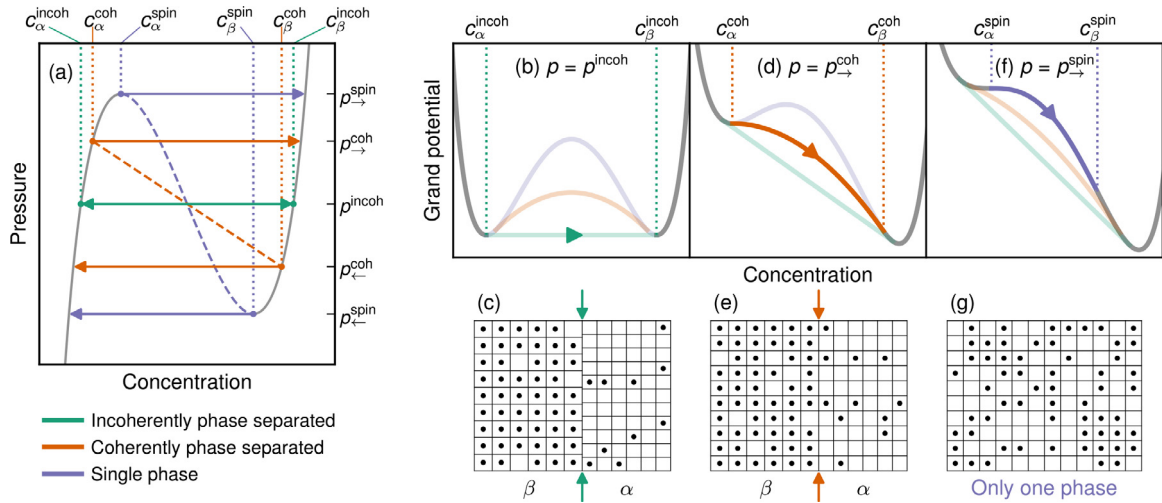


Fig. 1. Pathways for a phase transition in a generic open system. (a) The phase transition is characterized by a plateau in the pressure–composition isotherm. The plateau occurs, however, at different pressures depending on the pathway of the phase transition. (b) If the α/β interface is incoherent (as schematically depicted in (c)), the phase transition is thermodynamically allowed at $p = p^{\text{incoh}}$, where the two minima in the grand potential are equal. (d) If the α/β interface remains coherent during absorption (as in (e)), a higher pressure, $p = p^{\text{coh}}$, is required to overcome the strain energy barrier and induce the transition from α to β phase. (f) Absorption can in principle also occur with a continuously increasing but spatially homogeneous concentration (g), i.e., without the formation of two coexisting phases, if the pressure is increased to $p = p^{\text{spin}}$ (the spinodal). Upon desorption, the incoherent phase transition occurs at the same pressure as absorption, whereas in the coherent and single-phase phase cases, lower pressures are required, leading to (thermodynamic) hysteresis. Note that interface energies and kinetic effects (especially related to nucleation), which are ignored here, will generally lead to some degree of (kinetic) hysteresis also in the incoherent case.

ciples, which may otherwise rationalize experimental observations in terms of the underlying atomic-scale interactions.

Here, we remedy this situation by demonstrating a methodology that allows us to calculate the phase diagram, the hysteresis, and the interface energies for open, coherent systems using a model built on first-principles calculations. Notably, we obtain not only the incoherent but also the coherent and (incoherent) spinodal phase boundaries, and we demonstrate that the pathway of the phase transition changes character from coherent coexistence during the transition (Fig. 1d and e) to a spatially homogeneous single-phase configuration above approximately 400 K (Fig. 1f and g). Our approach is based on the use of density-functional theory (DFT) calculations for constructing an alloy cluster expansion (CE) that explicitly takes strain into account, we sample the system using Monte Carlo (MC) simulations in a constrained ensemble that allows for free energy integration inside the two-phase region, and we demonstrate how to analyze these simulations in order to extract the relevant thermodynamic quantities. While the individual parts of this approach are well-established, they have to the best of our knowledge not been combined previously. (In fact, a similar but simpler energy model was already constructed in 1979 to study the incoherent phase transition in Pd–H [35].) We anticipate that the results will aid the interpretation and prediction of hydride formation in Pd nanoparticles. The methodology is, however, not limited to Pd–H or even interstitial alloys, but can be applied to any alloy with a coherent phase transition between two phases with the same crystal structure.

2. Theory

2.1. Phase separation in closed systems

Our work focuses on an open system (Pd in an atmosphere of hydrogen), but we begin with a general analysis of the energetics of closed systems, since they are in some respects easier to understand. Consider a system with overall concentration c_{av} , phase separated coherently with interface orientation $\hat{\mathbf{k}}$ into the α and the β phases having, respectively, concentrations c_α and c_β . The

free energy of this phase-separated system can be written as

$$F_{\alpha/\beta}(c_{\text{av}}, \hat{\mathbf{k}}) = \min_{c_\alpha, c_\beta} \left\{ \underbrace{V_\alpha f_{\text{sp}}(c_\alpha) + V_\beta f_{\text{sp}}(c_\beta)}_{\text{bulk free energy}} + \underbrace{V e_{\text{strain}}(c_{\text{av}}, c_\alpha, c_\beta, \hat{\mathbf{k}})}_{\text{strain}} + \underbrace{A \gamma_{\alpha/\beta}(\hat{\mathbf{k}}, c_\alpha, c_\beta)}_{\text{interface}} \right\}. \quad (1)$$

Here, V_α and V_β are the volumes of the α and the β phases (which can be determined from conservation of the number of atoms or atomic sites), V the total volume ($V = V_\alpha + V_\beta$), $f_{\text{sp}}(c)$ the free energy per volume of the single-phase system at concentration c , $e_{\text{strain}}(c_{\text{av}}, c_\alpha, c_\beta, \hat{\mathbf{k}})$ the coherency strain energy per volume, A the area of the interface, and $\gamma_{\alpha/\beta}(\hat{\mathbf{k}}, c_\alpha, c_\beta)$ the interface energy. If the strain and the interface energy terms are excluded, the expression is minimized by the well-known common tangent construction. We will call the minimizing concentrations in this case the incoherent phase boundaries c_α^{incoh} and c_β^{incoh} , since they form the phase boundaries of the incoherently phase-separated system (in which the strain term vanishes).

In a coherently phase-separated system, the strain term does not vanish because the two phases need to adopt the same in-plane lattice parameter for the interface to be coherent. While the interface energy term (scaling with area) becomes insignificant in a sufficiently large system, the strain term remains important since it scales with volume. The free energy of a coherently phase-separated system is thus not additive; it is larger than the sum of its non-strained, constituent phases due to the additional strain energy mandated by the coherent interface. In general, the free energy $F_{\alpha/\beta}(c_{\text{av}}, \hat{\mathbf{k}})$ is therefore *not* minimized by the common tangent construction [14], but the concentrations c_α and c_β may be, respectively, larger and smaller than c_α^{incoh} and c_β^{incoh} [17,18]. We will refer to these minimizing concentrations as the coherent phase boundaries c_α^{coh} and c_β^{coh} since they form the phase boundaries of the coherent system. To summarize, in an incoherent system, there is phase separation for $c_\alpha^{\text{incoh}} < c_{\text{av}} < c_\beta^{\text{incoh}}$, whereas in a coherent system phase separation occurs for $c_\alpha^{\text{coh}} < c_{\text{av}} < c_\beta^{\text{coh}}$.

and these concentrations satisfy the conditions $c_{\alpha}^{\text{coh}} > c_{\alpha}^{\text{incoh}}$ and $c_{\beta}^{\text{coh}} < c_{\beta}^{\text{incoh}}$.

2.2. Phase transitions in open systems

The preceding analysis is helpful also for open systems (such as Pd in an atmosphere of hydrogen), for which a chemical potential μ is fixed and the number of solute atoms is allowed to vary. In such systems, the equilibrium state is given by the minimum in the grand potential, which can be written

$$\Omega = F - \mu Nc, \quad (2)$$

where F is the same free energy as in the closed system (by virtue of the equivalency of ensembles in the thermodynamic limit), N is the total number of available sites, and c the fraction of those sites that are occupied by an atom. In the incoherent system, the absorption and desorption phase transitions are in principle possible at the same chemical potential, corresponding to a pressure that we will refer to as p_{incoh} (Fig. 1a). The corresponding concentrations are equivalent to the incoherent phase boundaries and can be obtained by the common tangent construction for F or Ω (green line in Fig. 1b).

In the open, coherent system, on the other hand, the strain associated with coherent phase separation can be considered as a macroscopic energy barrier (Fig. 1d), as opposed to the microscopic interface energy that constitutes the barrier in incoherent systems. Such a macroscopic barrier cannot be overcome by fluctuations and therefore inevitably leads to a thermodynamic (i.e. non-kinetic) hysteresis [17,18] (Fig. 1a, orange lines). Consequently, the chemical potential needs to be increased (absorption) or decreased (desorption) beyond the incoherent equilibrium before the phase transition can proceed. In an open system, the coherent phase boundary can be understood as the concentration that has to be reached before the grand potential becomes monotonically decreasing from one phase to the other (Fig. 1d, orange line). These concentrations are the same as c_{α}^{coh} and c_{β}^{coh} described above in the context of closed systems. Below, we will show how the coherent phase boundaries can be extracted from Monte Carlo simulations.

It is worth emphasizing that coherent phase boundaries and spinodals are different; the latter are the concentrations at which the grand potential becomes monotonically decreasing in the direction of the phase transition, even with a spatially homogeneous distribution of solute atoms (Fig. 1f, purple line). The difference between the pressures corresponding to the spinodal concentrations in the open system will be referred to as full spinodal hysteresis (Fig. 1a, purple lines).

2.3. Finite simulation cells

Atomistic simulations are generally performed with simulation cells that are too small for interface contributions to be ignored, which leads to size-dependent results [36]. To better understand this, we make the approximation that the interface energy is independent of the concentrations of the two phases over some range close to c_{α} and c_{β} , and write $V = AL$ (where L is the length of the cell perpendicular to the interface). We can compare the free energy of the phase-separated system, $F_{\alpha/\beta}(c_{\text{av}}, \hat{\mathbf{k}})$, with the free energy of the single-phase system, $F_{\text{sp}}(c_{\text{av}})$. Phase separation occurs if and only if $F_{\alpha/\beta}(c_{\text{av}}, \hat{\mathbf{k}}) < F_{\text{sp}}(c_{\text{av}})$ and by rearrangement, using free energies per volume, this is equivalent to

$$\gamma_{\alpha/\beta}(\hat{\mathbf{k}}) < L[f_{\text{sp}}(c_{\text{av}}) - \tilde{f}_{\alpha/\beta}(c_{\text{av}}, \hat{\mathbf{k}})], \quad (3)$$

where $\tilde{f}_{\alpha/\beta}(c_{\text{av}}, \hat{\mathbf{k}})$ denotes the free energy per volume of the phase-separated system excluding the interface energy term. If the

strain energy term is sufficiently large, there will be no phase separation, because the expression on the right-hand side becomes negative. We will show that this occurs above a certain critical temperature T_c^{coh} in the Pd-H system. We note, however, that even below this critical temperature, a cell sufficiently large in the direction perpendicular to the interface is needed for phase separation to be energetically favorable. In a cell of finite length, phase separation will not occur in the full interval $c_{\alpha}^{\text{coh}} < c_{\text{av}} < c_{\beta}^{\text{coh}}$, but there will be intervals of concentrations above c_{α}^{coh} and below c_{β}^{coh} where a single-phase system is formed. The effect of interface energy in a small simulation cell is thus to narrow the two-phase region even further, although the concentrations of the constituent phases are unaffected (to a first approximation). As shown below, the results from simulations using cells of finite size can, however, be extrapolated to yield the coherent phase boundaries in the thermodynamic limit.

3. Methodology

3.1. DFT calculations

Energies were calculated with the projector augmented wave formalism as implemented in the Vienna ab initio simulation package (version 5.4.1, PAW 2015) [37,38] with the vdW-DF-cx exchange-correlation functional [39,40]. This functional was chosen due to its excellent performance for d-band metals [41], and we also note that it predicts a partial atomic volume for hydrogen that is closer to experiment than most commonly used functionals [42] (see Fig. S1). Wave functions were expanded in a plane wave basis set with a cutoff of 400 eV, the Brillouin zone (BZ) was sampled with a Γ -centered grid with a \mathbf{k} -point spacing of 0.2 \AA^{-1} , and occupations were set using Gaussian smearing with a width of 0.1 eV. Atomic positions and cell shape were relaxed until residual forces were below 25 meV/Å and stresses below 1 kbar. Once converged, we ran an additional single-point calculation with a \mathbf{k} -point spacing of 0.1 \AA^{-1} and the BZ integrations were carried out using the tetrahedron method with Blöchl corrections. In total, 368 different configurations were calculated, 30 of which were excluded from training and used as test set for the final CE model.

3.2. Alloy CEs with constituent strain

In a regular alloy CE, the energy of a structure with configuration σ is expanded in a sum of clusters α , each associated with an effective cluster interaction (ECI) J_{α} .

$$E_{\text{CE}}(\sigma) = J_0 + \sum_{\alpha} J_{\alpha} m_{\alpha} \langle \Pi_{\alpha}(\sigma) \rangle_{\alpha}. \quad (4)$$

Here, m_{α} is the number of clusters that are symmetrically equivalent to α and $\langle \Pi_{\alpha}(\sigma) \rangle_{\alpha}$ measures the average chemical order associated with the symmetrically equivalent clusters α . In our case,

$$\Pi_{\alpha} = \prod_{i \in \alpha} \Theta_i, \quad (5)$$

where the product runs over all sites in the cluster and $\Theta_i = 1$ if site i is occupied by a hydrogen atom, otherwise -1 . To construct a CE, the ECIs J_{α} need to be fitted. In practice, long-range clusters and clusters with many sites need to be truncated from Eq. (4). Here, we included pairs no longer than 1.9 lattice parameters apart and triplets in which the interatomic distances were no longer than 1.75 lattice parameters. The ECIs were obtained using automatic relevance determination regression [43] using the hyperparameter $\lambda = 10^4$. To exactly reproduce pure Pd ($c = 0$) and fully loaded Pd-H ($c = 1$), we constrained the zerolet J_0 and the singlet J_1 during fitting. The CE was created using the ICET package [44].

Long-ranged interactions mediated by strain are no longer captured after the CE has been truncated. In particular, the energetics of coherent interfaces in size-mismatched systems are qualitatively wrong. To overcome this limitation of a standard alloy CE, Laks et al. [45] proposed the inclusion of an additional term referred to as the constituent strain,

$$E(\sigma) = E_{CE}(\sigma) + E_{CS}(\sigma) \\ = E_{CE}(\sigma) + \sum_{\mathbf{k}} \Delta E_{CS}(\hat{\mathbf{k}}, c) F(\mathbf{k}, \sigma). \quad (6)$$

To find the ECIs, the second term is subtracted from the training data prior to fitting. The constituent strain term associates an energy with static concentration waves, i.e., concentrations that vary along a direction $\hat{\mathbf{k}}$. Superlattices formed as a result of phase separation are examples of such concentration waves. A superlattice is a structure in which n atomic layers of phase A are followed by n atomic layers of B, periodically repeated, and can be characterized by the orientation $\hat{\mathbf{k}}$ of the interface between the two phases. If the interface between the phases is coherent but the phases are size-mismatched, as is the case for the α and β phases of Pd-H, such superlattices are associated with an elastic strain energy. Since the stiffness is not isotropic, this energy depends on the orientation $\hat{\mathbf{k}}$ of the coherent interface. The term $\Delta E_{CS}(\hat{\mathbf{k}}, c)$ is a material property that can be calculated from a large number of small DFT calculations using the same parameters as described above (but without relaxation), following the approach outlined by Ozolins et al. [46]. It describes the excess energy (per atom) associated with superlattice formation in the $\hat{\mathbf{k}}$ direction having an overall concentration c . Specifically, it can be written

$$\Delta E_{CS}(\hat{\mathbf{k}}, c) = \min_{a_{SL}} \left[(1 - c) \Delta E_{Pd}^{epi}(a_{SL}, \hat{\mathbf{k}}) + c \Delta E_{PdH}^{epi}(a_{SL}, \hat{\mathbf{k}}) \right], \quad (7)$$

where the minimization is over the lattice parameter a_{SL} in the plane of the interface and $E_X^{epi}(a_{SL}, \hat{\mathbf{k}})$ represents the excess energy of phase X when it is epitaxially strained to the lattice parameter a_{SL} .

The factor $F(\mathbf{k}, \sigma)$ is a measure of the extent of configuration σ matching a concentration wave with reciprocal vector \mathbf{k} . Following more recent versions of this approach [47,48], we write it as

$$F(\mathbf{k}, \sigma) = |S(\mathbf{k}, \sigma)|^2 e^{-\eta |\mathbf{k}|^2} / 4c(1 - c), \quad (8)$$

where c is the concentration and $S(\mathbf{k}, \sigma)$ is the structure factor. The exponential term suppresses the constituent strain energy associated with rapidly varying concentrations, and we found that for the present system $\eta = 10 \text{ \AA}$ provides an accurate CE while the constituent strain is still well described.

Evaluation of the constituent strain involves a summation over \mathbf{k} -points in the first Brillouin zone of the primitive face-centered cubic (FCC) cell, and nonzero $F(\mathbf{k}, \sigma)$ are obtained for \mathbf{k} that are integer multiples of the reciprocal lattice vectors of the supercell. For each nonzero value $F(\mathbf{k}, \sigma)$, we need to know $\Delta E_{CS}(\hat{\mathbf{k}}, c)$ to evaluate the strain energy. For large simulation cells, this requires information about $\Delta E_{CS}(\hat{\mathbf{k}}, c)$ for a large number of crystal directions $\hat{\mathbf{k}}$. To avoid an excessive number of DFT calculations, we used a fit to the known values of $\Delta E_{CS}(\hat{\mathbf{k}}, c)$ to calculate constituent strain in unknown directions $\hat{\mathbf{k}}$ (for details, see Supplementary Note 3). Since low-index directions dominate the simulation cells employed in this work, the fitted values have only a marginal impact on the overall result.

3.3. Monte Carlo simulations in the VCSGC ensemble

To extract thermodynamic quantities using our model, we performed MC simulations using the MCHAMMER module of the ICET package [44]. To this end, we used a standard Metropolis algorithm

in which the chemical identity of a randomly chosen site is flipped with probability

$$P(\text{accept}) = \min \{1, \exp(-\Delta\psi/k_B T)\}. \quad (9)$$

The choice of ψ corresponds to sampling of different thermodynamic ensembles. In the present approach, we specifically need to access two-phase regions, where one value of the chemical potential maps to multiple concentrations. We therefore used the variance-constrained semi-grand canonical (VCSGC) ensemble [49,50], for which

$$\psi = E + \bar{\kappa} N k_B T (c_{av} + \bar{\phi}/2)^2, \quad (10)$$

where E is the potential energy, N the total number of sites, and c_{av} the overall concentration. The parameters $\bar{\phi}$ and $\bar{\kappa}$ constrain the average and the variance of the concentration, respectively. We used $\bar{\kappa} = 200$ throughout, but the simulations are quite insensitive to this choice. Simulations in the VCSGC ensemble allow for thermodynamic integration, since the (canonical) free energy derivative is an observable of the ensemble,

$$\frac{\partial F}{\partial c} = -2\bar{\kappa} N k_B T (\langle c_{av} \rangle + \bar{\phi}/2), \quad (11)$$

where $\langle c_{av} \rangle$ is the observed overall concentration, in the present case the one of hydrogen. By running a series of simulations in the range $-2 \lesssim \bar{\phi} \lesssim 0$, one can thereby continuously map out the relation between chemical potential and concentration over the entire interval $0 < \langle c_{av} \rangle < 1$. This in turn enables one to integrate the free energy over concentration. In contrast to the semi-grand canonical ensemble, the constraint on the concentration variance implies that simulations will stabilize also inside two-phase regions, and the free energy can be integrated across phase boundaries. The latter is a crucial ingredient in our method.

Furthermore, the observed state can be related to the chemical potential difference of the constituents. In our case, the constituents are hydrogen and vacancies, and with a zero chemical potential for vacancies, we can write

$$\bar{\mu}_H = \frac{1}{N} \frac{\partial F}{\partial c_{av}}. \quad (12)$$

For the present case, this quantity is related to the absolute chemical potential of H_2 gas according to $\mu_{H_2} = 2(\mu_H^0 + \bar{\mu}_H)$, where μ_H^0 is a reference that accounts for the offset introduced by fitting mixing energies rather than absolute energies. Assuming the H_2 gas is ideal, we can relate the chemical potential to the partial pressure of H_2 via

$$\mu_{H_2}(T, p_{H_2}) = \mu_{H_2}^0(T) + k_B T \ln \frac{p_{H_2}}{p_{H_2}^0}. \quad (13)$$

Since small errors in the temperature-dependent reference $\mu_{H_2}^0(T)$ have a large impact on the relation between μ_{H_2} and p , we chose to fit this reference level so as to reproduce the plateau pressure of the phase transition as measured in experiment (see Fig. S2). This is the only experimental input in our model. Our quantification of the hysteresis is, however, not impacted by this fit, only the absolute pressures for the transition from α to β phase and vice versa.

4. Results and discussion

4.1. Calculation of phase boundaries

To calculate phase boundaries, we begin by studying the free energy landscape obtained from MC simulations in simulation cells of increasing length, ranging in size from $4 \times 4 \times 4$ conventional (4-atom) unit cells (256 octahedral interstitial sites) to $4 \times 4 \times 35$ conventional unit cells (2,240 sites) using a CE with strain (for details concerning the CE model, see Supplementary Note 1, Fig. S3

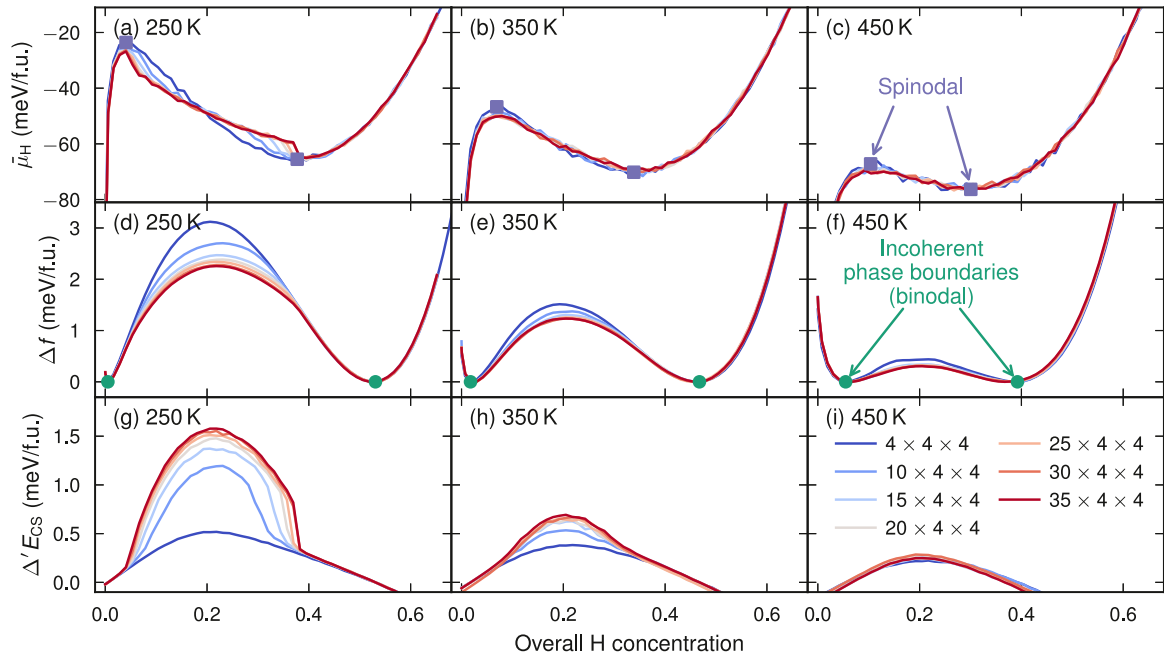


Fig. 2. Energetics of Pd-H based on MC simulations at 250 K (left), 350 K (middle), and 450 K (right) in cells elongated along $\langle 100 \rangle$. (a–c) $\bar{\mu}_H$ - c isotherms always coincide above and below the phase boundaries, but in the two-phase region at low temperatures the isotherm changes with simulation cell length. (d–f) The free energy decreases with increasing simulation cell length; yet it approaches a finite value inside the two-phase region, indicating a macroscopic energy barrier. The decrease with cell length is pronounced at low temperature but almost non-existent at high temperature. (g–i) The free energy barrier results from a combination of chemical free energy and strain energy, but the strain energy contribution is significant only in long cells at low temperatures, indicating that it is only in these cells that phase separation occurs. Here, the free energy f (d–f) and the strain energy E_{CS} (g–i) have been tilted (Δf and $\Delta'E_{CS}$) so as to be zero at the incoherent phase boundaries.

and Fig. S4). Our approach allows us to obtain the relationship between hydrogen chemical potential $\bar{\mu}_H$ and overall concentration c_{av} also in the two-phase $\alpha + \beta$ region, which is characterized by one value of $\bar{\mu}_H$ mapping to several values of c_{av} (Fig. 2a–c). By integration, we obtain the free energy $\Delta f(c_{av})$ (Fig. 2d–f, here tilted to make $\Delta f(c_{\alpha}^{incoh}) = \Delta f(c_{\beta}^{incoh}) = 0$). The $\alpha + \beta$ two-phase region is manifested by a concave interval in $\Delta f(c_{av})$. By drawing the common tangent, we can identify the *incoherent* phase boundaries, c_{α}^{incoh} and c_{β}^{incoh} (green circles in Fig. 2d–f). These are the equilibrium concentrations of an incoherently phase-separated system.

The identification of incoherent phase boundaries (the binodal) is insensitive to simulation cell size and shape, since free energies calculated with different simulation cells only differ inside the two-phase region. Nevertheless, these differences reflect important aspects of the simulations. At low temperatures, the chemical potential in the two-phase region (Fig. 2a, 250 K) is such that the free energy barrier becomes lower as the simulation cell grows longer (Fig. 2d). This is expected, since with a larger cell the system has greater configurational freedom and can thus explore more configurations. The main difference between the small, cubic cell and the long cells, is that the latter support phase separation. This is most clearly manifested by a larger strain energy inside the two-phase region in long cells than in the small, cubic cell (Fig. 2g). At 350 K (Fig. 2h), these effects are much less pronounced and at 450 K (Fig. 2i), they are non-existent; the strain energy is almost identical in the smallest and the largest cell. This indicates that phase separation does not occur, which is readily confirmed by inspection of the trajectories.

The *spinodal* lies inside the incoherent phase boundaries where the free energy depends on simulation cell size, and thus it cannot be deduced from an arbitrary simulation cell. To calculate the spinodal, we track, respectively, the position of the local maximum and minimum in the $\bar{\mu}_H$ - c_{av} isotherm for the smallest simulation cell (purple squares in Fig. 2a–c), because this is the only cell that

maintains the single-phase, homogeneous concentration profile required for the spinodal to be well-defined.

A few additional observations are helpful at this point. The $\bar{\mu}_H$ - c_{av} isotherm (Fig. 2a) converges fairly quickly as the simulation cell becomes longer. It does, however, not converge to the horizontal line connecting c_{α}^{incoh} and c_{β}^{incoh} (the common tangent) but to a sloping line with a weak curvature. Differences between cells of different length are largest close to the edges of the two-phase region, because phase separation is not necessarily favorable if the volume fraction of the minority phase is too small, an effect that becomes more pronounced the smaller the cell. The system then adopts a single-phase configuration, and the thermodynamic equilibrium state coincides with the small $4 \times 4 \times 4$ cell. As a result of the slope of the free energy derivative, the free energy barrier approaches a finite value; in other words, it does not vanish in the thermodynamic ($N \rightarrow \infty$) limit. This finite energy barrier is a consequence of the system being *coherently* phase separated. These observations are consistent with the model by Schwarz and Khachatryan [17,18].

To extract the *coherent* phase boundaries, we are interested in the compositions of the two phases in the coherently phase-separated system. To extract these, we calculated a running average of hydrogen concentration per atomic layer, with the average taken over five layers. We then calculated the hydrogen concentration in the α phase as the average concentration of the longest series of contiguous atomic layers that had a concentration below 20%, and similarly for the β phase (illustrated in Fig. 3a). The results show that the hydrogen concentration of the β phase increases as the β phase grows and the overall concentration increases (Fig. 3b). It is, however, always significantly smaller than c_{β}^{incoh} . In the α phase, the concentration is essentially constant but larger than c_{α}^{incoh} (Fig. 3c). As discussed above, phase separation is not necessarily favorable in finite simulation cells with overall concentrations close to the phase boundaries. Consequently,

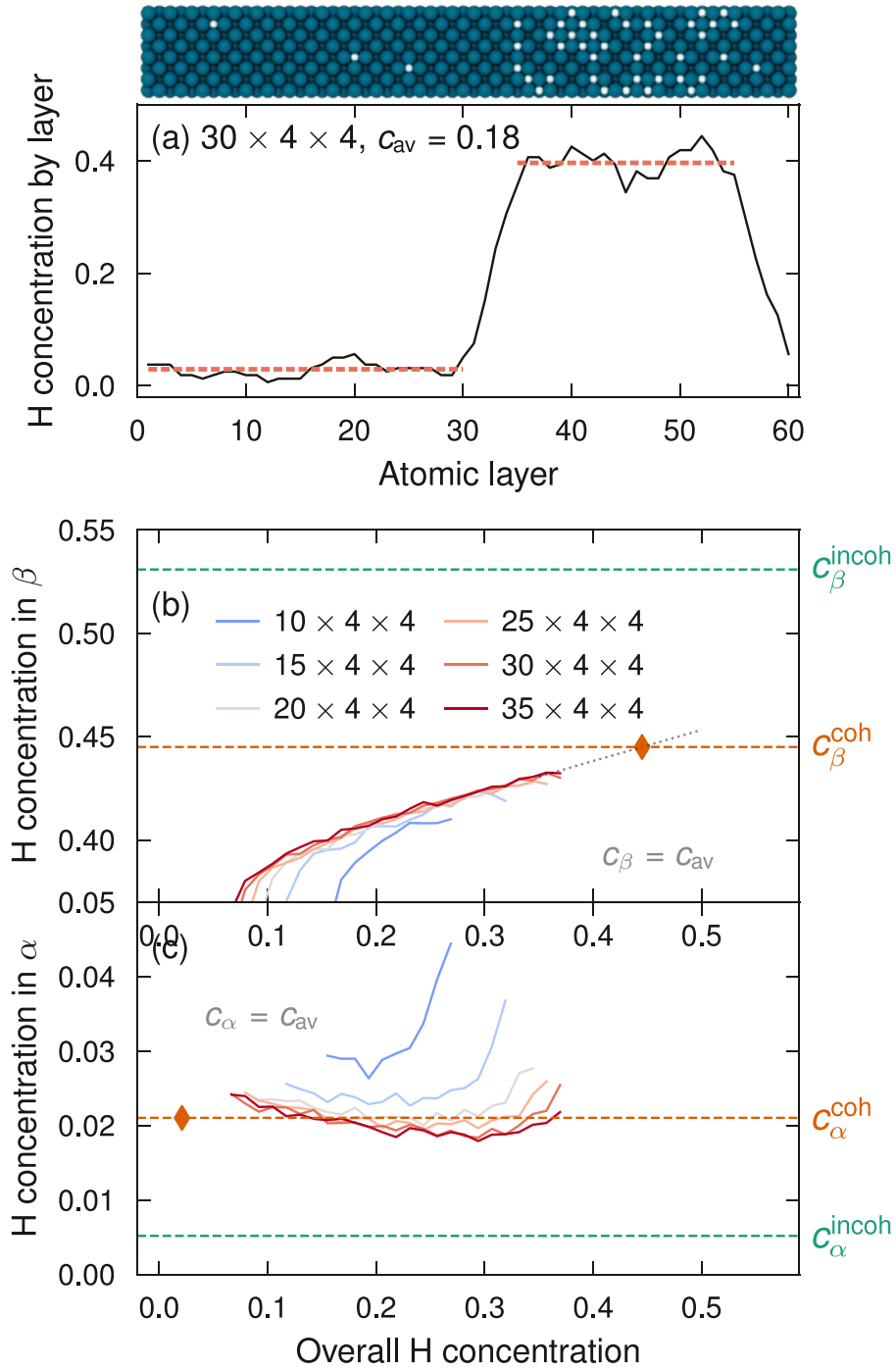


Fig. 3. Extraction of coherent phase boundaries. Data presented concerns {100} interfaces at 250 K, but the procedure is analogous for other interfaces and temperatures. (a) The hydrogen concentration in each atomic layer was calculated and averaged over five neighboring layers (black line), in this case for a snapshot of a $30 \times 4 \times 4$ simulation cell, having 60 atomic layers (inset, note that Pd atoms are fixed). The concentration in the α and the β phase was taken as the average concentration in the longest set of contiguous atomic layers that had, respectively, concentration below and above 0.2 (red, dashed line). (b) By averaging the thus obtained concentrations over all snapshots, using different overall concentrations, one observes that the concentration in the β phase is independent of simulation cell size for sufficiently long cells if the overall concentration is not too close to the phase boundaries. The concentration further increases as the β phase grows. By linear extrapolation (gray, dotted line) to 100% volume fraction β , where the overall concentration is equal to the concentration in the β phase, the coherent phase boundary c_{β}^{coh} is extracted (orange, dashed line). This concentration is significantly smaller than c_{β}^{incoh} (green, dashed line, as extracted in Fig. 2d–f). (c) In the α phase, the concentration is essentially unaffected by the overall concentration. The corresponding coherent phase boundary c_{α}^{coh} (orange, dashed line) is significantly larger than the incoherent phase boundary c_{α}^{incoh} (green, dashed line). (For interpretation of the references to color in this figure legend, the reader is referred to the web version of this article.)

our data for the composition of the α and the β phases do not reach the points where the concentration of the phase equals the overall concentration (i.e., where the volume fraction of the phase is 100%). Nevertheless, the available data enables extrapolation to these points (orange diamonds in Fig. 3b and c). These points yield

the coherent phase boundaries at the corresponding temperature, c_{α}^{coh} and c_{β}^{coh} , because they mark the limits of the concentration interval in which coherent phase coexistence is favorable in the closed system, or, equivalently, the limits where the grand potential becomes monotonically decreasing in the direction of the

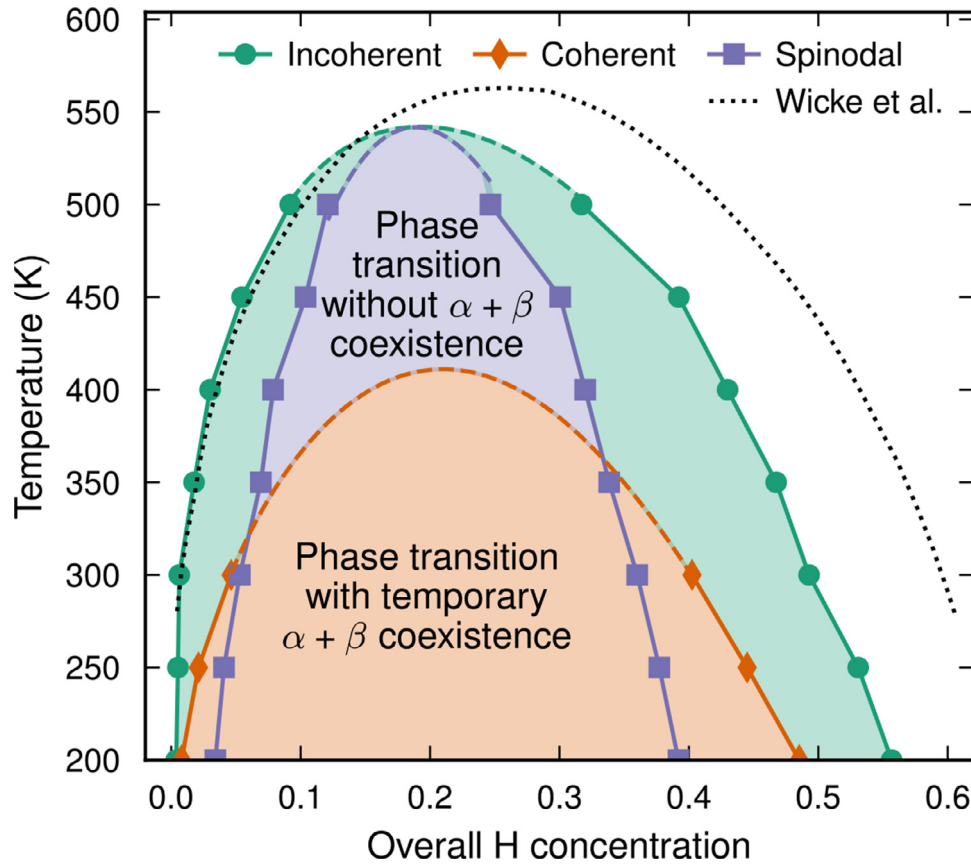


Fig. 4. Phase diagram for Pd-H. The incoherent phase boundaries (binodals, green lines) indicate where the phase transition is thermodynamically favorable in the stress-free case. The critical temperature agrees well with experimental results (540 K in our model, 560 K experimentally [51]), and so does the phase boundary on the α side, while the concentration in the β phase is underestimated compared to experiment. If the phase transition occurs fully coherently, phase coexistence between α and β during the transition is only favorable between the coherent phase boundaries (orange area). Above approximately 400 K, coherent phase coexistence is no longer a favorable pathway for any composition, and the phase transition from α to β and vice versa proceeds with a spatially homogeneous hydrogen concentration in the full concentration range. This phase transition becomes spontaneous within the incoherent spinodal (purple area). Dashed lines indicate extrapolation of the results of the simulations. (For interpretation of the references to color in this figure legend, the reader is referred to the web version of this article.)

phase transition in the open system (in the thermodynamic limit). We emphasize that the coherent and incoherent phase boundaries differ significantly. We also note that, in the present system, it is sufficient to consider simulation cells with {100} interfaces when calculating coherent phase boundaries, since any other orientation leads to larger strain energy (see Fig. S4) and thereby thermodynamically less favorable coherent phase coexistence.

4.2. The Pd-H phase diagram

By tracking the incoherent and coherent phase boundaries as well as the spinodal as a function of temperature, we can construct the phase diagram (Fig. 4). We note first that the critical temperature predicted by our model (540 K) agrees well with the experimental data by Wicke et al. [51], while noting that the critical temperature obtained with a CE is in general associated with a significant statistical uncertainty [44,52]. The incoherent phase boundary (green line) marks the concentrations where the phase transition may start if it is fully incoherent. Compared to experiment (taken from desorption isotherms of bulk samples, which are believed to be close to the actual incoherent phase boundaries [51]), the phase boundary on the α side is in very good agreement, while we underestimate the concentration on the β side. Similar results for the incoherent phase diagram have previously been obtained in CE studies [52,53]. Differences between simulation and experiment are likely related to both the (in)accuracy of the underlying DFT calculations and the treatment of temperature-dependent proper-

ties, notably the neglect of vibrations. A series of harmonic models for low-energy structures fitted with the HIPHIVE package [54], indicate that vibrations may move the phase boundary to higher concentrations, closer to experiment (Fig. S5).

The coherent phase boundaries (orange line in Fig. 4) mark the concentrations where the fully coherent phase transition may start; Inside these boundaries, phase transitions may occur with the two phases temporarily coexisting with a coherent interface. The coherent phase boundaries are always inside the incoherent phase boundaries because of the additional strain energy contribution. Coherent phase separation between α and β becomes energetically unfavorable above approximately 400 K, because then the strain energy associated with phase separation is always larger than the gain in chemical free energy. We will refer to this as the coherent critical temperature. The exact value of the coherent critical temperature is difficult to determine accurately and was here obtained by extrapolation of the coherent phase boundaries in the range of 200–300 K where the constitution of the phases is still relatively easy to determine. The value of 400 K obtained by this procedure is further supported by an analysis of the histogram of atomic layer concentrations (Fig. S6). Our calculated coherent critical temperature is higher than the only previous attempt to determine the coherent critical temperature in Pd-H that we are aware of [55]. Based on experimental data for elastic constants, lattice parameters, and incoherent critical temperature, the latter gave an estimate for the coherent critical temperature between approximately 260 and 350 K.

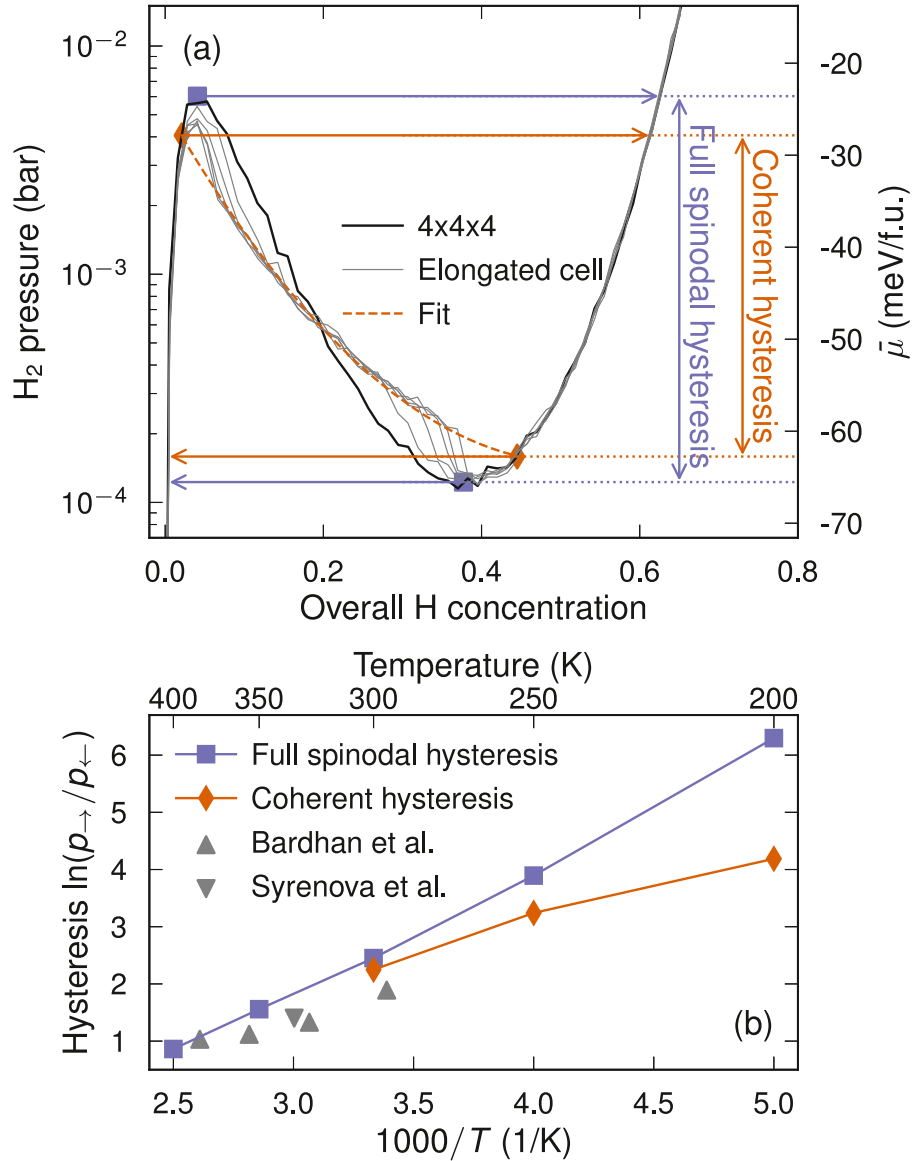


Fig. 5. Thermodynamic hysteresis in the coherent Pd-H system. (a) p - c isotherm at 250 K. We identify two kinds of hysteresis, full spinodal hysteresis (purple lines) and coherent hysteresis (orange lines), i.e., the thermodynamic hysteresis intrinsic to the coherent phase transition. The former is derived by finding the local maximum and minimum in the isotherm, whereas the latter requires extrapolation to the thermodynamic (infinite size) limit (orange, dashed line). (b) Coherent hysteresis is smaller than full spinodal hysteresis as long as the coherent phase boundary lies outside the spinodal ($\lesssim 350$ K), but for higher temperatures the hysteresis will always be full spinodal (unless dislocations form). Compared to measurements on nanoparticles [20,24] (gray triangles), we make a slight overestimation of the hysteresis, possibly because of defect formation during dehydrogenation in experiment. Hysteresis is here quantified as the logarithm of the ratio between the transition pressure from α to β (p_{\rightarrow}) and β to α (p_{\leftarrow}). (For interpretation of the references to color in this figure legend, the reader is referred to the web version of this article.)

We thus predict that there is an interval between approximately 400 K and 540 K where the phase transition occurs without $\alpha + \beta$ coexisting during the transition. In this interval, the phase transition does not proceed by nucleation and growth, since nucleation would be associated with a strain energy that exceeds the gain in chemical free energy. Instead, the system will always remain in a single-phase configuration (as schematically indicated in Fig. 1g). We emphasize that the transition from α to β (and vice versa) is still a first-order phase transition in this temperature interval, and is as such characterized by a plateau in the absorption/desorption isotherm as well as hysteresis. The behavior of the system above and below 400 K only differs with regard to the pathway of the phase transition.

We have also drawn the incoherent spinodal in Fig. 4 (purple line). As discussed in Section 2.2, the significance of the incoherent spinodal in an open, coherent system is that it marks the concen-

trations where the chemical potential of hydrogen is large (small) enough for any free energy barrier for absorption (desorption) to be eliminated (as indicated in Fig. 1f). Hence, the phase transition will always occur spontaneously once the incoherent spinodal has been reached. (We also acknowledge the existence of the coherent spinodal, where the coherent system becomes unstable with respect to formation of concentration waves, but it is not relevant for our analysis.)

4.3. Calculation of hysteresis

Equipped with the coherent phase boundaries, we can now extrapolate the coherent energy landscape to the thermodynamic limit. To this end, we fit a second degree polynomial (orange, dashed line in Fig. 5a) to μ_{H} as a function of c_{av} for the longest cells in the concentration interval [0.1, 0.3], while enforcing that

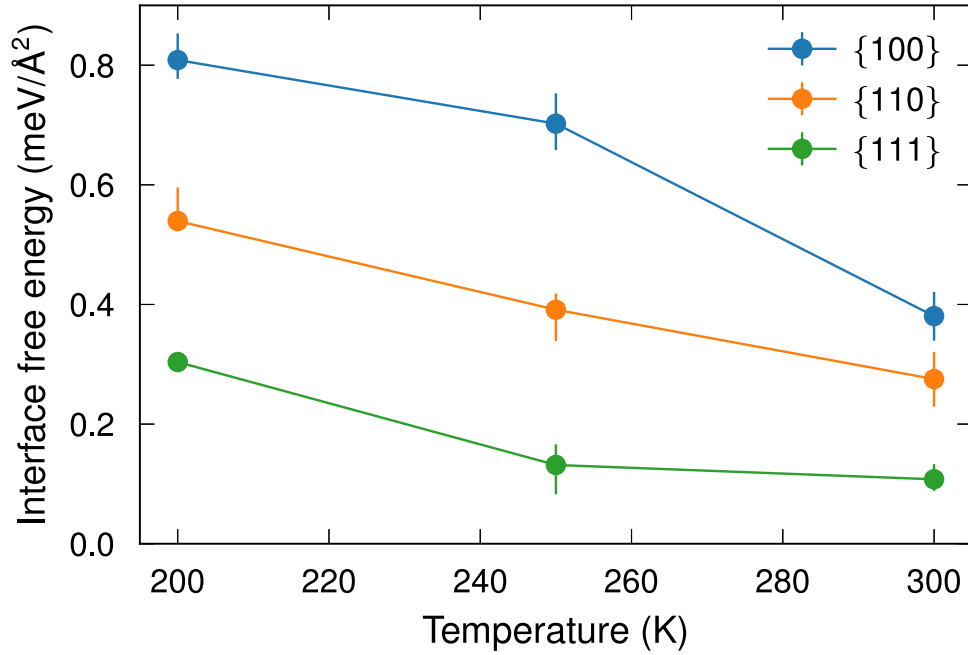


Fig. 6. Coherent α/β interface free energies in Pd-H. The interface energies are the largest for interfaces with {100} orientation and smallest for {111}. The error bars represent the spread of interface energies over the (overall) concentration interval [0.15, 0.25], and the symbols the average in that interval.

the resulting curve crosses the single-phase $\bar{\mu}_H$ - c_{av} curve (black line in Fig. 5a) at the concentrations c_{α}^{coh} and c_{β}^{coh} calculated in the previous section. The (thermodynamic, coherent) hysteresis is then given by the pressure difference between the highest and lowest points on this line; this is the path of lowest free energy in the thermodynamic limit. Below approximately 350 K, this hysteresis is smaller than the full spinodal hysteresis, which is given by the difference between the maximum and the minimum of the black line in Fig. 5a. When the spinodal lies outside the coherent phase boundaries, the system will always undergo full spinodal hysteresis; the system cannot lower its free energy by phase separation outside the coherent phase boundaries. Using the full spinodal hysteresis as an approximation of the coherent hysteresis, as has previously been done in the literature [6,56], is thus sensible if the temperature is sufficiently high.

We quantify the hysteresis using $\ln p_{\rightarrow}/p_{\leftarrow}$, where p_{\rightarrow} and p_{\leftarrow} are the transition pressures from α to β and vice versa (Fig. 5b). We note that our hysteresis is significantly narrower than the hysteresis predicted by Schwarz et al. [56] (for example, at 300 K we obtain a coherent hysteresis $\ln p_{\rightarrow}/p_{\leftarrow} \approx 2.3$, which is less than half of what was predicted in [56]). We attribute the majority of this difference to the choice of the underlying atomic scale interaction model, as a semi-empirical embedded atom method potential was used in Schwarz et al. [56].

Comparison of our results to the hysteresis experimentally measured in Pd nanoparticles smaller than 300 nm, which are widely considered to transition coherently, is not entirely straight-forward, since the hysteresis decreases with the size of the nanoparticles. This is connected to the critical temperature also decreasing with smaller nanoparticle size [6], an effect that our model does not take into account. Moreover, modeling of hydrogen insertion into Pd nanoparticles using an empirical potential has shown that pressure-composition isotherms can be qualitatively different between bulk and small nanoparticles due to a large fraction of surface and subsurface sites in the latter [57]. To enable a fair comparison, we extracted experimental data for two cases where the hysteresis was measured at fixed temperature for single-crystalline nanocubes of different sizes [20,24], and extrapolated the size-

dependent hysteresis to the bulk limit (gray triangles in Fig. 5b, extrapolation in Fig. S7). Our model still slightly overestimates the hysteresis compared to these data. Previous analyses have indicated that the $\alpha \rightarrow \beta$ phase transition occurs fully coherently in Pd nanoparticles, whereas this does not always apply for the $\beta \rightarrow \alpha$ transition [6,8]. If desorption is at least partially incoherent, the hysteresis will shrink, which may explain the discrepancy between the hysteresis in our model and experiment, as our model assumes fully coherent phase transitions during both loading and unloading. It should further be noted that the surfaces of nanoparticles allow for stress relaxation, in particular far from the α/β interface, which most likely leads to a lowering of the free energy barrier of the phase transition associated with coherency stresses. It is possible that the extrapolation to the bulk limit corrects for this effect to some extent, but not necessarily completely. The overestimation of the hysteresis is very slight and is thus not necessarily a sign that dislocations form during hydrogenation. We also note that quantitative deviations of the phase boundary on the β side between our results and experiment may propagate into errors in the hysteresis.

Finally, we note that the results in Fig. 5 were obtained with simulation cells with {100} interfaces; any other orientation would yield a larger coherent hysteresis, since the strain is the smallest for interfaces with {100} interfaces (as quantified in Fig. S4). This does not necessarily mean that the phase transition will always proceed with a {100} phase front, because interface energies may be smaller in other directions. Interface energies are, however, by definition not taken into account for the thermodynamically mandated coherent hysteresis.

4.4. Calculation of interface free energies

While interface free energies do not impact coherent hysteresis in the thermodynamic limit, they are in practice expected to play a role for the actual phase transition, as they constitute a microscopic energy barrier that needs to be overcome. Our simulations allow us to extract the coherent interface free energies as well (for methodological details, see Supplementary Note 2 and Fig. S8). The results show that the interface energy of {100} is larger than both

{111} and {110} (Fig. 6). Hence, while strain favors a phase transition dominated by {100} interfaces, the (chemical) interface energies favor other interface orientations. It should be noted that the lower interface energies of {111} and {110} are not necessarily only an effect of favorable chemistry. The concentrations of the constituent phases vary between the three interface orientations, since different interfaces strike different balances between chemistry and strain energy. Nevertheless, the impact of interface energies is to stabilize {111} and {110} interfaces relative to {100}, which may provide a clue as to why the former interfaces have been routinely observed experimentally during hydrogenation of Pd nanoparticles [25]. We note, however, that the interface energies are small in absolute terms; unless the nucleus size is less than a few nanometers, the free energy barrier (Fig. 2d) will be completely dominated by strain.

5. Conclusion

We have found that the combination of alloy CEs including strain and MC simulations in a constrained ensemble with cells of different sizes and shapes, constitutes a robust methodology for extracting the most relevant thermodynamic quantities of coherent phase transitions in an open system. Most importantly the present approach enables one to quantitatively predict not only the incoherent phase boundaries and the (incoherent) spinodal, but also the coherent phase boundaries, using only input from first-principles calculations. The results are consistent with the theory of Schwarz and Khachatryan [17,18] with only small qualitative differences, such as composition dependence of the constituent phases in the coherently phase-separated system (Fig. 3b) and a weak curvature in the $\bar{\mu}_{\text{H-C}}$ isotherm in the miscibility gap (Fig. 5a). Such differences are not unexpected given that the real system deviates slightly from the simplifying assumptions in this theory. For example, the variation of the compositions in the phase-separated system is likely the result of a small but significant deviation from Vegard's rule (Fig. S1) as well as the concentration dependence of the elastic constants (Fig. S9), which have been shown to impact the dependence of phase composition on overall composition [31,58–60].

The phase diagram for Pd–H computed here (Fig. 4) reveals that there is an interval between approximately 400 K and 540 K where the phase transition proceeds with a hydrogen distribution that is at all times homogeneous throughout the material, without any formation of two coexisting phases. To the best of our knowledge, no direct, experimental observations of such a phase transition in Pd–H has been reported yet, which is not surprising given that *in situ* imaging has been restricted to much lower temperatures [8,25]. There is experimental evidence for phase coexistence close to the (incoherent) critical temperature in bulk samples [61], but production of dislocations can be expected in such samples [62,63], and our result is only valid if interfaces stay fully coherent. We cannot rule out that this assumption may be violated also in nanoparticles, for which most experimental evidence for coherent phase transitions has been obtained at temperatures well below the incoherent critical temperature [6,7]. Our result does, however, urge caution: conclusions drawn about the dynamics of the phase transition at low temperatures may not be applicable at higher temperatures, since they may occur by different processes.

Our approach allows for quantification of the hysteresis, both above 350 K where it is fully spinodal, and below 350 K where it is anywhere between fully spinodal and coherent. The results are largely consistent with available experimental data, although comparison is not straight-forward due to the size-dependency of hysteresis in nanoparticles. We reemphasize that the present results are applicable to fully coherent phase separation in Pd–H and thus mostly applicable to nanoparticles with diameters below 300 nm

[6,7]. We note that if defects (notably dislocations) are formed, which is expected in bulk Pd–H, other models such as the one in Ref. [64] are better suited to describe hysteresis. The latter model, however, relies on interface pinning and is therefore not suitable to analyze hysteresis in single-crystalline nanoparticles.

Finally, using extrapolation of data from simulation cells with varying shapes, interface free energies can be calculated. In the present case, the interface free energies are very small, which is not unexpected given that a condition for coherent phase transitions to be competitive, is that their interface free energies are lower than the incoherent interface free energies. For most purposes, the interface free energies of Pd–H are small enough to be safely ignored; the direction-dependent strain energy is by far the dominant term unless the nucleus size is smaller than a few nanometers. Yet, these interface energies may play a role in the pathway of the hydrogenation of Pd nanoparticles, which has been observed to occur, at least sometimes, via interface geometries disfavored by strain but favored by interface free energies [25].

Declaration of Competing Interest

The authors declare that they have no known competing financial interests or personal relationships that could have appeared to influence the work reported in this paper.

Acknowledgments

This work was funded by the Knut and Alice Wallenberg Foundation (grant number 2015.0055), the Swedish Research Council (grant numbers 2015-04153, 2018-06482, 2020-04935), and the Swedish Foundation for Strategic Research (grant number RMA15-0052). The computations were enabled by resources provided by the Swedish National Infrastructure for Computing (SNIC) at NSC, HPC2N and PDC partially funded by the Swedish Research Council (grant number 2018-05973). We thank Prof. Mark Asta and Dr. Babak Sadigh for insightful discussions.

Supplementary material

Supplementary material associated with this article can be found, in the online version, at doi:[10.1016/j.actamat.2022.117697](https://doi.org/10.1016/j.actamat.2022.117697).

References

- [1] X. Zhang, M. Van Hulzen, D.P. Singh, A. Brownrigg, J.P. Wright, N.H. Van Dijk, M. Wagemaker, Direct view on the phase evolution in individual LiFePO₄ nanoparticles during Li-ion battery cycling, *Nat. Comm.* 6 (1) (2015) 1–7, doi:[10.1038/ncomms9333](https://doi.org/10.1038/ncomms9333).
- [2] A. Schneemann, J.L. White, S. Kang, S. Jeong, L.F. Wan, E.S. Cho, T.W. Heo, D. Prendergast, J.J. Urban, B.C. Wood, M.D. Allendorf, V. Stavila, Nanostructured metal hydrides for hydrogen storage, *Chem. Rev.* 118 (22) (2018) 10775–10839, doi:[10.1021/acs.chemrev.8b00313](https://doi.org/10.1021/acs.chemrev.8b00313).
- [3] C. Wadell, S. Syrenova, C. Langhammer, Plasmonic hydrogen sensing with nanostructured metal hydrides, *ACS Nano* 8 (12) (2014) 11925–11940, doi:[10.1021/nn505804f](https://doi.org/10.1021/nn505804f).
- [4] I. Darmadi, F.A.A. Nugroho, C. Langhammer, High-performance nanostructured palladium-based hydrogen sensors: current limitations and strategies for their mitigation, *ACS Sens.* 5 (11) (2020) 3306–3327, doi:[10.1021/acssensors.0c02019](https://doi.org/10.1021/acssensors.0c02019).
- [5] M. Rahimpour, F. Samimi, A. Babapoor, T. Tohidian, S. Mohebi, Palladium membranes applications in reaction systems for hydrogen separation and purification: a review, *Chem. Eng. and Proc.* 121 (2017) 24–49, doi:[10.1016/j.ccep.2017.07.021](https://doi.org/10.1016/j.ccep.2017.07.021).
- [6] R. Griessen, N. Strohheldt, H. Giessen, Thermodynamics of the hybrid interaction of hydrogen with palladium nanoparticles, *Nat. Mater.* 15 (3) (2016) 311–317, doi:[10.1038/nmat4480](https://doi.org/10.1038/nmat4480).
- [7] A. Ulvestad, M.J. Welland, W. Cha, Y. Liu, J.W. Kim, R. Harder, E. Maxey, J.N. Clark, M.J. Highland, H. You, P. Zapol, S.O. Hruszkewycz, G.B. Stephenson, Three-dimensional imaging of dislocation dynamics during the hydriding phase transformation, *Nat. Mater.* 16 (5) (2017) 565–571, doi:[10.1038/nmat4842](https://doi.org/10.1038/nmat4842).
- [8] T.C. Narayan, F. Hayee, A. Baldi, A.L. Koh, R. Sinclair, J.A. Dionne, Direct visualization of hydrogen absorption dynamics in individual palladium nanoparticles, *Nat. Commun.* 8 (1) (2017) 1–8, doi:[10.1038/ncomms14020](https://doi.org/10.1038/ncomms14020).

- [9] J.W. Cahn, Coherent fluctuations and nucleation in isotropic solids, *Acta Metall.* 10 (10) (1962) 907–913, doi:[10.1016/0001-6160\(62\)90140-2](https://doi.org/10.1016/0001-6160(62)90140-2).
- [10] F. Larché, J.W. Cahn, A linear theory of thermochemical equilibrium of solids under stress, *Acta Metall.* 21 (8) (1973) 1051–1063, doi:[10.1016/0001-6160\(73\)90021-7](https://doi.org/10.1016/0001-6160(73)90021-7).
- [11] F. Larché, J.W. Cahn, A nonlinear theory of thermochemical equilibrium of solids under stress, *Acta Metall.* 26 (1) (1978) 53–60, doi:[10.1016/0001-6160\(78\)90201-8](https://doi.org/10.1016/0001-6160(78)90201-8).
- [12] R.O. Williams, Long-period superlattices in the copper-gold system as two-phase mixtures, *Metall. Trans. A* 11 (2) (1980) 247–253, doi:[10.1007/BF02660629](https://doi.org/10.1007/BF02660629).
- [13] R.O. Williams, The calculation of coherent phase equilibria, *Calphad* 8 (1) (1984) 1–14, doi:[10.1016/0364-5916\(84\)90024-5](https://doi.org/10.1016/0364-5916(84)90024-5).
- [14] J.W. Cahn, F. Larché, A simple model for coherent equilibrium, *Acta Metall.* 32 (11) (1984) 1915–1923, doi:[10.1016/0001-6160\(84\)90173-1](https://doi.org/10.1016/0001-6160(84)90173-1).
- [15] W.C. Johnson, P.W. Voorhees, Phase equilibrium in two-phase coherent solids, *Metall. Trans. A* 18 (7) (1987) 1213–1228, doi:[10.1007/BF02647191](https://doi.org/10.1007/BF02647191).
- [16] Z.-K. Liu, J. Ågren, On two-phase coherent equilibrium in binary alloys, *Acta Metall. Mater.* 38 (4) (1990) 561–572, doi:[10.1016/0956-7151\(90\)90210-8](https://doi.org/10.1016/0956-7151(90)90210-8).
- [17] R.B. Schwarz, A.G. Khachatryan, Thermodynamics of open two-phase systems with coherent interfaces, *Phys. Rev. Lett.* 74 (13) (1995) 2523–2526, doi:[10.1103/PhysRevLett.74.2523](https://doi.org/10.1103/PhysRevLett.74.2523).
- [18] R.B. Schwarz, A.G. Khachatryan, Thermodynamics of open two-phase systems with coherent interfaces: application to metal-hydrogen systems, *Acta Mater.* 54 (2) (2006) 313–323, doi:[10.1016/j.actamat.2005.08.044](https://doi.org/10.1016/j.actamat.2005.08.044).
- [19] D. Wang, T.B. Flanagan, T. Kuji, Hysteresis scans for Pd–H and Pd-alloy–H systems, *Phys. Chem. Chem. Phys.* 4 (2002) 4244–4254, doi:[10.1039/B201271P](https://doi.org/10.1039/B201271P).
- [20] R. Bardhan, L.O. Hedges, C.L. Pint, A. Javey, S. Whitelam, J.J. Urban, Uncovering the intrinsic size dependence of hydriding phase transformations in nanocrystals, *Nat. Mater.* 12 (10) (2013) 905–912, doi:[10.1038/nmat3716](https://doi.org/10.1038/nmat3716).
- [21] C. Wadell, T. Pingel, E. Olsson, I. Zorić, V.P. Zhdanov, C. Langhammer, Thermodynamics of hydride formation and decomposition in supported sub-10 nm Pd nanoparticles of different sizes, *Chem. Phys. Lett.* 603 (2014) 75–81, doi:[10.1016/j.cplett.2014.04.036](https://doi.org/10.1016/j.cplett.2014.04.036).
- [22] A. Baldi, T.C. Narayan, A.L. Koh, J.A. Dionne, In situ detection of hydrogen-induced phase transitions in individual palladium nanocrystals, *Nat. Mater.* 13 (12) (2014) 1143–1148, doi:[10.1038/nmat4086](https://doi.org/10.1038/nmat4086).
- [23] C. Langhammer, V.P. Zhdanov, I. Zorić, B. Kasemo, Size-dependent hysteresis in the formation and decomposition of hydride in metal nanoparticles, *Chem. Phys. Lett.* 488 (1) (2010) 62–66, doi:[10.1016/j.cplett.2010.01.071](https://doi.org/10.1016/j.cplett.2010.01.071).
- [24] S. Syrenova, C. Wadell, F.A. Nugroho, T.A. Gschneidner, Y.A.D. Fernandez, G. Nalin, D. Świtlik, F. Westerlund, T.J. Antosiewicz, V.P. Zhdanov, et al., Hydride formation thermodynamics and hysteresis in individual Pd nanocrystals with different size and shape, *Nat. Mater.* 14 (12) (2015) 1236–1244, doi:[10.1038/nmat4409](https://doi.org/10.1038/nmat4409).
- [25] K. Sytwu, F. Hayee, T.C. Narayan, A.L. Koh, R. Sinclair, J.A. Dionne, Visualizing facet-dependent hydrogenation dynamics in individual palladium nanoparticles, *Nano Lett.* 18 (9) (2018) 5357–5363, doi:[10.1021/acs.nanolett.8b00736](https://doi.org/10.1021/acs.nanolett.8b00736).
- [26] D.A. Cogswell, M.Z. Bazant, Coherency strain and the kinetics of phase separation in LiFePO₄ nanoparticles, *ACS Nano* 6 (3) (2012) 2215–2225, doi:[10.1021/nn204177u](https://doi.org/10.1021/nn204177u).
- [27] D.A. Cogswell, M.Z. Bazant, Theory of coherent nucleation in phase-separating nanoparticles, *Nano Lett.* 13 (7) (2013) 3036–3041, doi:[10.1021/nl400497t](https://doi.org/10.1021/nl400497t).
- [28] M. Tang, A. Karma, Surface modes of coherent spinodal decomposition, *Phys. Rev. Lett.* 108 (2012) 265701, doi:[10.1103/PhysRevLett.108.265701](https://doi.org/10.1103/PhysRevLett.108.265701).
- [29] A.T. Phan, A.E. Gheribi, P. Chartrand, Modeling of coherent phase transformation and particle size effect in LiFePO₄ cathode material and application to the charging/discharging process, *Electrochim. Acta* 295 (2019) 632–644, doi:[10.1016/j.electacta.2018.10.185](https://doi.org/10.1016/j.electacta.2018.10.185).
- [30] A.T. Phan, A.E. Gheribi, P. Chartrand, Coherent and para-equilibrium phase transformations in Mn-doped-LiFePO₄ cathode materials: implications for lithium ion battery performances, *J. Alloys Compd.* 838 (2020) 155550.
- [31] S. Chen, C. Li, Z. Du, C. Guo, C. Niu, Overall composition dependences of coherent equilibria, *Calphad* 37 (2012) 65–71, doi:[10.1016/j.calphad.2012.01.005](https://doi.org/10.1016/j.calphad.2012.01.005).
- [32] R. Spatschek, G. Gobbi, C. Hüter, A. Chakrabarty, U. Aydin, S. Brinckmann, J. Neugebauer, Scale bridging description of coherent phase equilibria in the presence of surfaces and interfaces, *Phys. Rev. B* 94 (2016) 134106, doi:[10.1103/PhysRevB.94.134106](https://doi.org/10.1103/PhysRevB.94.134106). <https://link.aps.org/doi/10.1103/PhysRevB.94.134106>
- [33] J.W. Doak, C. Wolverton, Coherent and incoherent phase stabilities of thermo-electric rocksalt IV–VI semiconductor alloys, *Phys. Rev. B* 86 (2012) 144202, doi:[10.1103/PhysRevB.86.144202](https://doi.org/10.1103/PhysRevB.86.144202).
- [34] M. Sumita, Y. Tanaka, M. Ikeda, T. Ohno, Theoretically designed Li₃PO₄ (100)/LiFePO₄ (010) coherent electrolyte/cathode interface for all solid-state Li ion secondary batteries, *J. Phys. Chem. C* 119 (1) (2015) 14–22, doi:[10.1021/jp5060342](https://doi.org/10.1021/jp5060342).
- [35] S. Dietrich, H. Wagner, Model calculation for the incoherent phase-transition in the palladium-hydrogen system, *Z. Phys. B Cond. Matter* 36 (2) (1979) 121–126, doi:[10.1007/BF01320212](https://doi.org/10.1007/BF01320212).
- [36] D. Sheppard, P. Xiao, W. Chmielewski, D.D. Johnson, G. Henkelman, A generalized solid-state nudged elastic band method, *J. Chem. Phys.* 136 (7) (2012) 074103, doi:[10.1063/1.3684549](https://doi.org/10.1063/1.3684549).
- [37] G. Kresse, J. Furthmüller, Efficiency of ab-initio total energy calculations for metals and semiconductors using a plane-wave basis set, *Comput. Mater. Sci.* 6 (1) (1996) 15–50, doi:[10.1016/0927-0256\(96\)00008-0](https://doi.org/10.1016/0927-0256(96)00008-0).
- [38] G. Kresse, D. Joubert, From ultrasoft pseudopotentials to the projector augmented-wave method, *Phys. Rev. B* 59 (1999) 1758–1775, doi:[10.1103/PhysRevB.59.1758](https://doi.org/10.1103/PhysRevB.59.1758).
- [39] M. Dion, H. Rydberg, E. Schröder, D.C. Langreth, B.I. Lundqvist, Van der Waals density functional for general geometries, *Phys. Rev. Lett.* 92 (2004) 246401, doi:[10.1103/PhysRevLett.92.246401](https://doi.org/10.1103/PhysRevLett.92.246401).
- [40] K. Berland, P. Hyldgaard, Exchange functional that tests the robustness of the plasmon description of the van der Waals density functional, *Phys. Rev. B* 89 (2014) 035412, doi:[10.1103/PhysRevB.89.035412](https://doi.org/10.1103/PhysRevB.89.035412).
- [41] L. Gharraee, P. Erhart, P. Hyldgaard, Finite-temperature properties of nonmagnetic transition metals: comparison of the performance of constraint-based semilocal and nonlocal functionals, *Phys. Rev. B* 95 (2017) 085147, doi:[10.1103/PhysRevB.95.085147](https://doi.org/10.1103/PhysRevB.95.085147). <https://link.aps.org/doi/10.1103/PhysRevB.95.085147>
- [42] S.S. Setayandeh, T. Gould, A. Vaez, K. McLennan, N. Armanet, E. Gray, First-principles study of the atomic volume of hydrogen in palladium, *J. Alloys Compd.* 864 (2021) 158713, doi:[10.1016/j.jallcom.2021.158713](https://doi.org/10.1016/j.jallcom.2021.158713).
- [43] F. Pedregosa, G. Varoquaux, A. Gramfort, V. Michel, B. Thirion, O. Grisel, M. Blondel, P. Prettenhofer, R. Weiss, V. Dubourg, J. Vanderplas, A. Passos, D. Cournapeau, M. Brucher, M. Perrot, E. Duchesnay, Scikit-learn: machine learning in Python, *J. Mach. Learn. Res.* 12 (2011) 2825–2830.
- [44] M. Ångqvist, W.A. Muñoz, J.M. Rahm, E. Fransson, C. Durniak, P. Rozyczko, T.H. Rod, P. Erhart, ICET—A Python library for constructing and sampling alloy cluster expansions, *Adv. Theory Simul.* 2 (7) (2019) 1900015, doi:[10.1002/adts.201900015](https://doi.org/10.1002/adts.201900015).
- [45] D.B. Laks, L.G. Ferreira, S. Froyen, A. Zunger, Efficient cluster expansion for substitutional systems, *Phys. Rev. B* 46 (1992) 12587–12605, doi:[10.1103/PhysRevB.46.12587](https://doi.org/10.1103/PhysRevB.46.12587).
- [46] V. Ozoliņš, C. Wolverton, A. Zunger, Effects of anharmonic strain on the phase stability of epitaxial films and superlattices: applications to noble metals, *Phys. Rev. B* 57 (1998) 4816–4828, doi:[10.1103/PhysRevB.57.4816](https://doi.org/10.1103/PhysRevB.57.4816).
- [47] J.Z. Liu, G. Trimarchi, A. Zunger, Strain-minimizing tetrahedral networks of semiconductor alloys, *Phys. Rev. Lett.* 99 (2007) 145501, doi:[10.1103/PhysRevLett.99.145501](https://doi.org/10.1103/PhysRevLett.99.145501).
- [48] J.Z. Liu, A. Zunger, Thermodynamic states and phase diagrams for bulk-incoherent, bulk-coherent, and epitaxially-coherent semiconductor alloys: application to cubic (Ga,In)_n, *Phys. Rev. B* 77 (2008) 205201, doi:[10.1103/PhysRevB.77.205201](https://doi.org/10.1103/PhysRevB.77.205201).
- [49] B. Sadigh, P. Erhart, Calculation of excess free energies of precipitates via direct thermodynamic integration across phase boundaries, *Phys. Rev. B* 86 (2012) 134204, doi:[10.1103/PhysRevB.86.134204](https://doi.org/10.1103/PhysRevB.86.134204).
- [50] B. Sadigh, P. Erhart, A. Stukowski, A. Caro, E. Martinez, L. Zepeda-Ruiz, Scalable parallel Monte Carlo algorithm for atomistic simulations of precipitation in alloys, *Phys. Rev. B* 85 (2012) 184203, doi:[10.1103/PhysRevB.85.184203](https://doi.org/10.1103/PhysRevB.85.184203).
- [51] E. Wicke, J. Blaurock, New experiments on and interpretations of hysteresis effects of Pd–D₂ and Pd–H₂, *J. Less Common Metals* 130 (1987) 351–363, doi:[10.1016/0022-5088\(87\)90129-9](https://doi.org/10.1016/0022-5088(87)90129-9).
- [52] J.M. Rahm, J. Löfgren, E. Fransson, P. Erhart, A tale of two phase diagrams: interplay of ordering and hydrogen uptake in Pd–Au–H, *Acta Mater.* 211 (2021) 116893, doi:[10.1016/j.actamat.2021.116893](https://doi.org/10.1016/j.actamat.2021.116893).
- [53] N. Bourgeois, P. Cenedese, J.-C. Crivello, J.-M. Joubert, Pd–H and Ni–H phase diagrams using cluster variation method and Monte Carlo simulation, *Philos. Mag.* 99 (19) (2019) 2376–2392, doi:[10.1080/14786435.2019.1628367](https://doi.org/10.1080/14786435.2019.1628367).
- [54] F. Eriksson, E. Fransson, P. Erhart, The hiphive package for the extraction of high-order force constants by machine learning, *Adv. Theory Simul.* 2 (5) (2019) 1800184, doi:[10.1002/adts.201800184](https://doi.org/10.1002/adts.201800184).
- [55] E. Ho, H.A. Goldberg, G.C. Weatherly, F.D. Manchester, An in situ electron microscope study of precipitation in palladium-hydrogen alloys, *Acta Metall.* 27 (5) (1979) 841–853, doi:[10.1016/0001-6160\(79\)90119-6](https://doi.org/10.1016/0001-6160(79)90119-6).
- [56] R.B. Schwarz, A.K. Khachatryan, A. Caro, M.I. Baskes, E. Martinez, Coherent phase decomposition in the Pd–H system, *J. Mater. Sci.* 55 (11) (2020) 4864–4882, doi:[10.1007/s10853-019-04179-z](https://doi.org/10.1007/s10853-019-04179-z).
- [57] E.A. Crespo, M. Ruda, S. Ramos de Debiaggi, E.M. Bringa, F.U. Braschi, G. Bertolino, Hydrogen absorption in Pd nanoparticles of different shapes, *Int. J. Hydrog. Energy* 37 (19) (2012) 14831–14837, doi:[10.1016/j.ijhydene.2011.12.075](https://doi.org/10.1016/j.ijhydene.2011.12.075).
- [58] M.J. Pfeifer, P.W. Voorhees, Coherent phase equilibrium in alloys with congruent particles, *Metall. Trans. A* 22 (9) (1991) 1921–1935, doi:[10.1007/BF02669860](https://doi.org/10.1007/BF02669860).
- [59] J.K. Lee, W. Tao, Coherent phase equilibria: effect of composition-dependent elastic strain, *Acta Metall. Mater.* 42 (2) (1994) 569–577, doi:[10.1016/0956-7151\(94\)90511-8](https://doi.org/10.1016/0956-7151(94)90511-8).
- [60] D. Korbacher, J. Von Pezold, S. Brinckmann, J. Neugebauer, C. Hüter, R. Spatschek, Modeling of phase equilibria in Ni–H: bridging the atomistic with the continuum scale, *Metals* 8 (4) (2018) 280, doi:[10.3390/met8040280](https://doi.org/10.3390/met8040280).
- [61] A.J. Maeland, T.R. Gibb Jr, X-ray diffraction observations of the Pd–H system through the critical region, *J. Phys. Chem.* 65 (7) (1961) 1270–1272, doi:[10.1021/j100825a501](https://doi.org/10.1021/j100825a501).
- [62] M. Wise, J. Farr, I. Harris, X-ray studies of the α/β miscibility gaps of some palladium solid solution-hydrogen systems, *J. Less Common Metals* 41 (1) (1975) 115–127, doi:[10.1016/0022-5088\(75\)90099-5](https://doi.org/10.1016/0022-5088(75)90099-5).
- [63] E. Wu, E. Kisi, E.M.A. Gray, Modelling dislocation-induced anisotropic line broadening in Rietveld refinements using a Voigt function. II. Application to neutron powder diffraction data, *J. Appl. Crystallogr.* 31 (3) (1998) 363–368, doi:[10.1107/S0021889897012181](https://doi.org/10.1107/S0021889897012181).
- [64] N.J. Weadock, P.W. Voorhees, B. Fultz, Interface pinning causes the hysteresis of the hydride transformation in binary metal hydrides, *Phys. Rev. Mater.* 5 (2021) 013604, doi:[10.1103/PhysRevMaterials.5.013604](https://doi.org/10.1103/PhysRevMaterials.5.013604).